Differential Cross Sections for Rotational Excitation of ND_3 by Ne†

Jeffrey J. Kay,‡ Sebastiaan Y. T. van de Meerakker,§ Elisabeth A. Wade,|| Kevin E. Strecker,*,‡ and David W. Chandler*,‡

Sandia National Laboratories, Livermore, California 94550, Fritz-Haber-Institut der Max-Planck-Gesellschaft, Faradayweg 4-6, 14195 Berlin, Germany, and Department of Chemistry and Physics, Mills College, Oakland, California

Received: May 27, 2009; Revised Manuscript Received: July 22, 2009

We report the first measured differential cross sections for rotationally inelastic collisions between ND_3 and Ne, obtained using velocity-mapped ion imaging. In these experiments, ND_3 molecules initially in the $J = 0$, $K = 0$ and $J = 1$, $K = 1$ quantum states collide with Ne atoms at a center-of-mass collision energy of 65 meV, leading to rotational excitation of ND_3. Differential cross sections are then determined from images of the rotationally excited scattered molecules using an iterative extraction method. These measurements complement and compare well with previous measurements of differential cross sections for the ammonia−rare gas system (Meyer, H. *J. Chem. Phys.* **1994**, *101*, 6697.; Meyer, H. *J. Phys. Chem.* **1995**, *99*, 1101.) and are also relevant to the production of cold ND_3 molecules by crossed-beam scattering (Kay, J. J.; van de Meerakker, S. Y. T.; Strecker, K. E.; Chandler, D. W. *Faraday Discuss.* **2009**, DOI: 10.1039/B819256C).

I. Introduction

Velocity-mapped ion imaging[1,2] has proven to be a very powerful tool in state- and angle-resolved molecular beam scattering measurements.[3−8] The singular advantage of this technique is that scattered species are detected at all angles simultaneously, which provides immunity to many of the sources of noise inherent in point-to-point measurements. This also allows data to be acquired very rapidly: measurements that would have taken days or weeks in the past can often now be completed in less than 1 h. This ability to rapidly measure high-quality state- and angle-resolved cross sections has allowed interrogation of collision dynamics at an unprecedented level of detail.[5−8]

Although molecular beam scattering experiments have a very rich history, complete sets of differential cross sections are available for only a limited number of scattering systems.[4] Extensive differential cross sections for collisions involving polyatomic molecules are rare. In this paper, we present differential cross sections for rotationally inelastic collisions between ND_3 and Ne. These are the first reported differential cross sections for the ND_3/Ne system and complement previous work on the related NH_3/He and NH_3/Ar systems.[12−14] The ND_3/Ne system is particularly interesting from the point of view of collisional cooling:[15−19] since the collision partners are of equal mass, it is possible to produce very cold samples of ND_3 molecules in a variety of quantum states by crossed-beam scattering.[19] Aside from providing sensitive information about the ammonia/neon potential energy surface, the differential cross sections we present here are therefore also useful in designing collisional cooling experiments and optimizing the production of cold ND_3 molecules.

II. Experiment

Our experiments are performed in a 90° crossed-beam scattering apparatus (described in ref 9) in which the scattered products are detected using velocity-mapped ion imaging. The scattering apparatus is divided into several vacuum chambers: two "source" chambers, two "differential" chambers, and one "scattering" chamber, all of which are separately pumped. Pulsed atomic and molecular beams are produced in the two source chambers by home-built piezoelectrically actuated pulsed valves containing either a 5% mixture of ND_3 in neon (at a total pressure of 40 psig) or pure neon (at a pressure of 80 psig). The pulsed valves operate at a repetition rate of 30 Hz and emit pulses approximately 150 μs in length. The center velocities of the ND_3 and Ne beams are measured to be 850 and 790 m/s, respectively. Typical rotational temperatures of the molecular beam are 5−10 K. Each beam passes through a 0.8 mm nickel skimmer (Beam Dynamics, Inc.) as it crosses from its respective source chamber into its respective differential chamber, and passes through a 0.8 mm collimating hole as it crosses into the scattering chamber. The two beams intersect in the scattering chamber, between two annular electrodes and along the axis of a time-of-flight imaging detector. All chambers are equipped with turbomolecular pumps and maintain typical base pressures of 10^{-8} Torr when the pulsed valves are off. The pressure in the scattering chamber is typically 10^{-7} Torr when the pulsed valves are operating.

The velocity distribution of the scattered ND_3 molecules (for a particular quantum state) is measured using velocity-mapped ion imaging. Molecules are state-selectively ionized by resonant absorption of two identical photons through the $\tilde{B}$ state. Discussion of the spectroscopic details of the $\tilde{B}-\tilde{X}$ transition in ND_3 can be found in refs 20 and 21 and references therein. In ND_3, all rovibrational levels of the $\tilde{X}$ ground state have nonzero spin-statistical weight and are doubled by inversion. The symmetry of the ground and excited electronic states and spin statistics of the three deuterium nuclei conveniently separate transitions originating from the two inversion components of the ground state into an alternating pattern: only transitions

† Part of the "Vincenzo Aquilanti Festschrift".

* To whom correspondence should be addressed. E-mail: K.E.S., kstreck@sandia.gov, D.W.C., chand@sandia.gov.

‡ Sandia National Laboratories.

§ Fritz-Haber-Institut der Max-Planck-Gesellschaft.

|| Mills College.

10.1021/jp904983w
Published on Web 08/20/2009

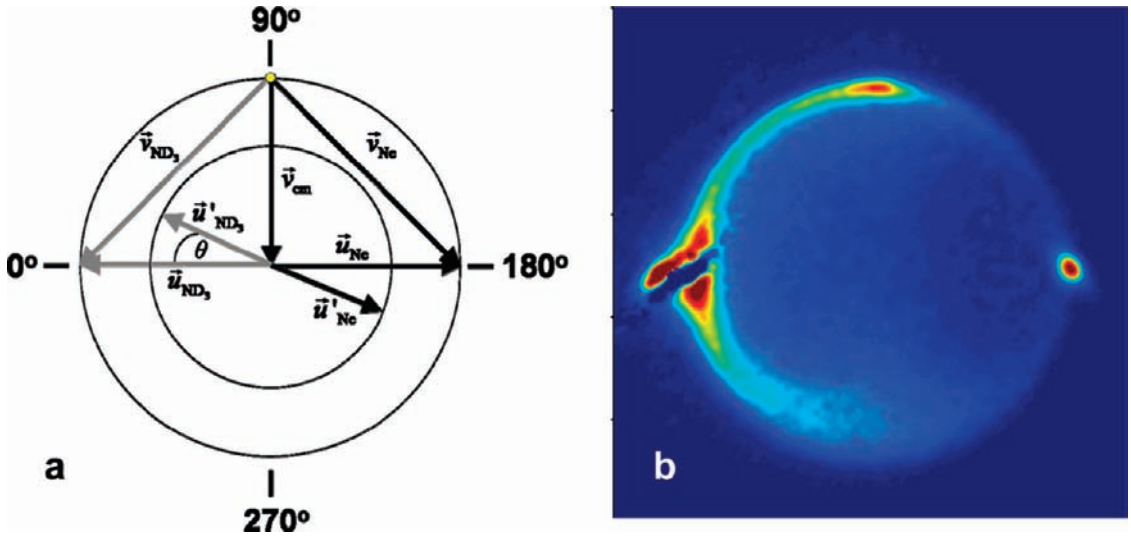

Figure 1. (a) Newton diagram for ND_3/Ne scattering. Unprimed vectors represent precollision quantities, primes represent postcollision quantities. (b) Experimental image of scattered molecules in the $J = 2$, $K = 0$ state.

originating from the *lower* inversion component of the ground state appear in bands in which ν_2 (the number of quanta of vibration in the "umbrella" mode of the excited state) is *even*, and only transitions from the *upper* inversion component appear in those bands in which ν_2 is *odd*. To monitor the upper and lower inversion components, we choose respectively the $\tilde{B}(5)$ and $\tilde{B}(4)$ bands, as these appear with reasonable intensity due to favorable Franck−Condon overlap between the upper and lower quantum states. Due to nuclear spin considerations and the low rotational temperature of the molecular beam, most ND_3 molecules are left in either the $J = 0$, $K = 0$ or $J = 1$, $K = 1$ states, with only a few percent of molecules occupying higher rotational levels. The molecules exist in two nuclear spin configurations, ortho and para, which do not interconvert by collisions or absorption of radiation and are cooled independently of one another. The spin considerations consequently pose a restriction on the collision dynamics: molecules in the $(J, K) = (0, 0)$ state only scatter into rotational states with $K = 3n$ (0, 3, 6, ...), and molecules in the $(J, K) = (1, 1)$ state only scatter into rotational states with $K = 3n + 1$ or $K = 3n + 2$ (1, 2, 4, 5, 7, 8, ...). It must be noted that, because the ion optics are set for velocity-mapped conditions, the entire experiment takes place in a static 500 V/cm electric field, which leads to mixing of levels of opposite parity. The cross sections we obtain here are therefore "parity-averaged".

Radiation of 315−325 nm wavelength for excitation of the two-photon transition is produced by frequency-doubling the output of a tunable pulsed dye laser (Lambda-Physik Scanmate, 5−7 ns pulse length, 0.1 cm^{-1} bandwidth) operating with DCM dye (Exciton, Inc.) using a KDP crystal (Inrad). The dye laser is pumped by the 532 nm output of a pulsed Nd:YAG laser (Coherent Infinity). The frequency-doubled output of the dye laser is focused by a spherical lens into the collision volume, coplanar with and bisecting the atomic and molecular beams. ND_3^+ ions produced by this laser pulse are then accelerated through the ion optics toward an imaging detector. The voltages applied to the electrodes comprising the ion optic assembly are set for velocity-mapping conditions, which maps each velocity component onto a unique spatial position on the detector. The detector itself consists of two microchannel plates arranged in a chevron configuration, placed before a phosphor screen. The voltage applied to the front plate of the detector is pulsed, producing a narrow mass gate which admits signal due to ND_3^+ and discriminates against undesired signals produced by other ions. Images of the phosphor screen are acquired by a thermoelectrically cooled CCD camera (Princeton Instruments, 1024 × 1024 pixels, cooled to −50 °C), continuously throughout the experiment, typically 5 s per exposure, for a total of 225 exposures. An automated background subtraction program runs continuously throughout the experiment, and alternates the timing of the atomic beam such that on even-numbered exposures both the atomic and molecular beams are most intense when the laser fires, and on odd-numbered exposures the atomic beam arrives several milliseconds after the laser fires while the timing of the molecular beam remains constant. The odd-numbered exposures are then subtracted from the even-numbered exposures to reduce systematic noise and eliminate the portion of the signal due to rotationally hot unscattered molecules in the molecular beam.

III. Results and Discussion

A Newton diagram describing the collision dynamics is shown in Figure 1. In the figure, $\vec{v}_{ND_3}$ and $\vec{v}_{Ne}$ represent the laboratory-frame velocities of ND_3 and Ne, $\vec{u}_{ND_3}$ and $\vec{u}_{Ne}$ represent their precollision center-of-mass velocities, and $\vec{u}'_{ND_3}$ and $\vec{u}'_{Ne}$ represent their postcollision center-of-mass velocities. The vector $\vec{v}_{cm}$ represents the velocity of the center-of-mass in the laboratory frame, and the scattering angle is denoted θ. During elastic collisions, there is no interconversion of kinetic and internal energy, and thus elastically scattered products are distributed along a ring of radius $|u'_{ND_3}| = |u'_{Ne}|$. During inelastic collisions, internal (rotational) excitation of the molecule occurs, and some kinetic energy is converted into rotational energy. The velocities of the scattered products are therefore lower, and inelastically scattered species are distributed along a smaller ring whose radius decreases with increasing rotational excitation. In all of our images, products scattered at 0° appear at the left of the image, and products scattered at 180° appear at right.

A typical image from the experiment is shown in Figure 1b, which depicts the distribution of scattered molecules in the $(J, K) = (3,3)$ state. The four prominent features in the image are (i) a ring of radius $|u'_{ND_3}|$, whose intensity at any point is proportional to the number of molecules detected at that particular scattering angle, (ii) an irregularly shaped "beam spot" at 0°, from unscattered ND_3 molecules in the (3, 3) state that

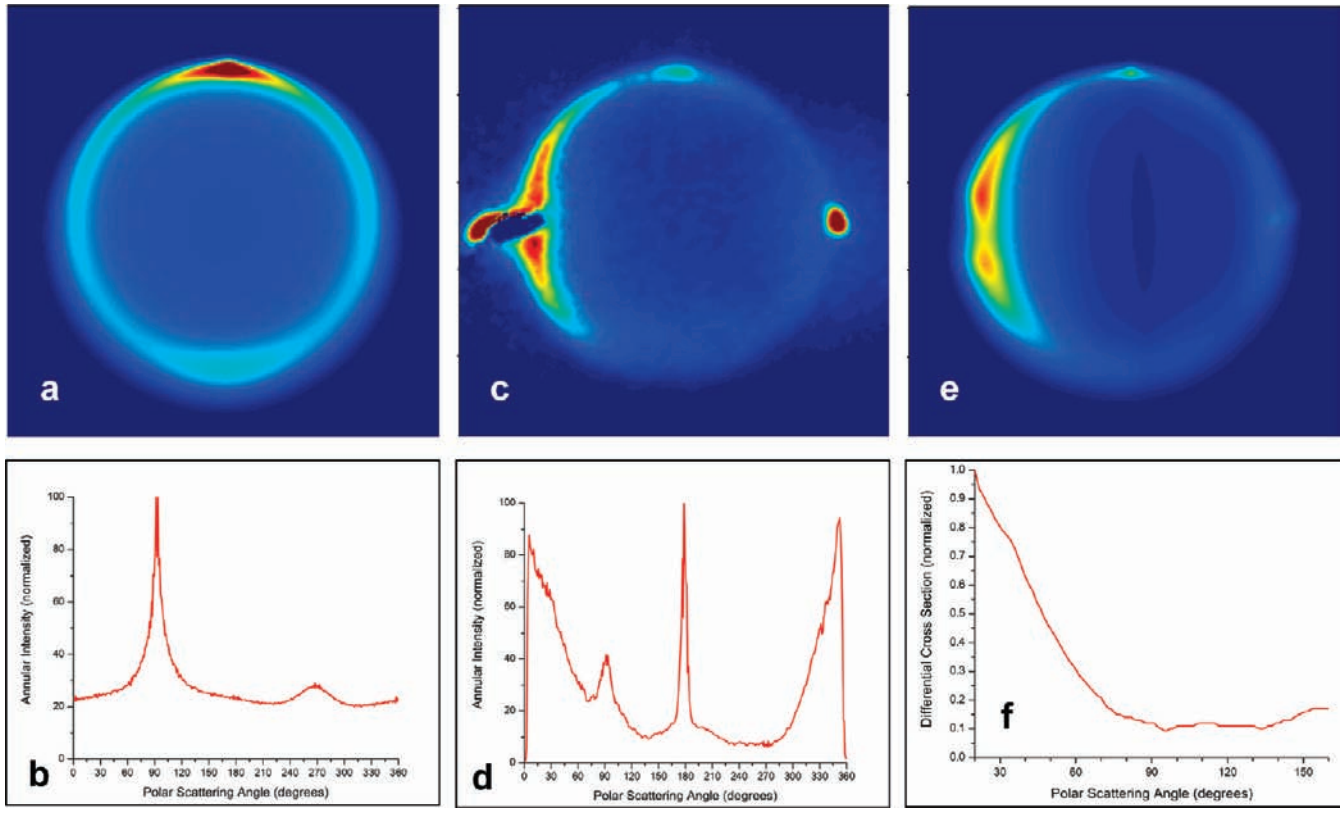

Figure 2. (a) Instrument function appropriate for $J = 0$, $K = 0$ $J = 3$, $K = 3$ scattering. (b) Annular intensity of instrument function. (c) Experimental image of scattered molecules in the $J = 3$, $K = 3$ state. (d) Annular intensity of experimental image. (e) Simulated image produced after four iterations. (f) Extracted differential cross section.

are present in the parent molecular beam, (iii) a second elliptical "beam spot" at 180°, which appears in our images due to residual ammonia in the valve that normally emits pure neon, and (iv) an area of high intensity along the ring of inelastically scattered products, near $\theta = 90°$, due to molecules with low laboratory-frame velocities, which preferentially accumulate in the scattering volume over time.

Although *qualitative* velocity distributions of the scattered molecules can be determined directly by inspection of the raw images, the extraction of quantitative differential cross sections is complicated by several factors.[9] First, as feature iv above implies, not all molecules are detected with equal efficiency: because the detection laser beam is focused in two dimensions and has a finite spatial width, the probability with which a given scattered molecule will be ionized and detected depends on both its direction of motion and the point in time at which it was scattered. Slower molecules tend to accumulate in the laser focus over the duration of the molecular beam pulses, whereas faster molecules tend to quickly escape detection. Scattered molecules propagating forward in the laboratory along the axis of the laser beam (i.e., near $\theta = 270°$) also tend to remain within the focal volume of the laser. Species scattered near 90° (and to a lesser extent, those scattered near 270°) are therefore detected with much greater efficiency than those scattered at other angles. Second, because of the nonzero velocity distributions of the molecular beams, both ND_3 and Ne appear with a *range* of initial velocities, and the image we obtain in our experiments is therefore not adequately described by a single Newton diagram, but instead corresponds to a superposition of *many* Newton diagrams differing slightly in the velocities of the two collision partners. This leads to an angle-dependent velocity distribution in the scattered products: all Newton spheres intersect at 90°, leading to a narrow velocity distribution in this direction, whereas the spheres are most widely separated at 270°, leading to a wide velocity distribution at this scattering angle. The scattering "rings" we observe in our images therefore tend to be sharper at the top of the image and more diffuse near the bottom. Third, the Doppler profile of the laser affects the detection efficiency: since the center frequency of the laser is adjusted and optimized by observing the ion signal from the residual rotationally excited molecules present in the molecular beam, scattered molecules with velocity components along the laser axis similar to the molecular beams (i.e., scattered molecules near the vertical center of the image) absorb radiation from the center of the frequency distribution of the laser (where the laser has maximum intensity) and are detected with greatest efficiency. Molecules whose velocity component along the laser axis are much lower or much higher (i.e., scattered molecules near the top or bottom of the image) absorb from the wings of the frequency distribution of the laser and are detected with lower efficiency. Finally, since both "beam spots" at least partially overlap some portion of the scattering ring, it is often difficult to determine accurate differential cross sections near 0° and 180°.

To account for these effects and determine quantitative differential cross sections, our laboratory has developed an iterative extraction method[9,10] based on the repeated comparison of a simulated image with the experimental image. (An alternate extraction method, developed by McBane,[11] has been shown to compare favorably with the DCS extraction method employed here and in refs 9 and 10.) The process begins with the construction of an appropriate "instrument function", which is itself a baseline simulated image in which the molecules are assumed to be scattered isotropically. The annular intensity of the experimental image is divided by the annular intensity of this instrument function, giving a first approximation to the

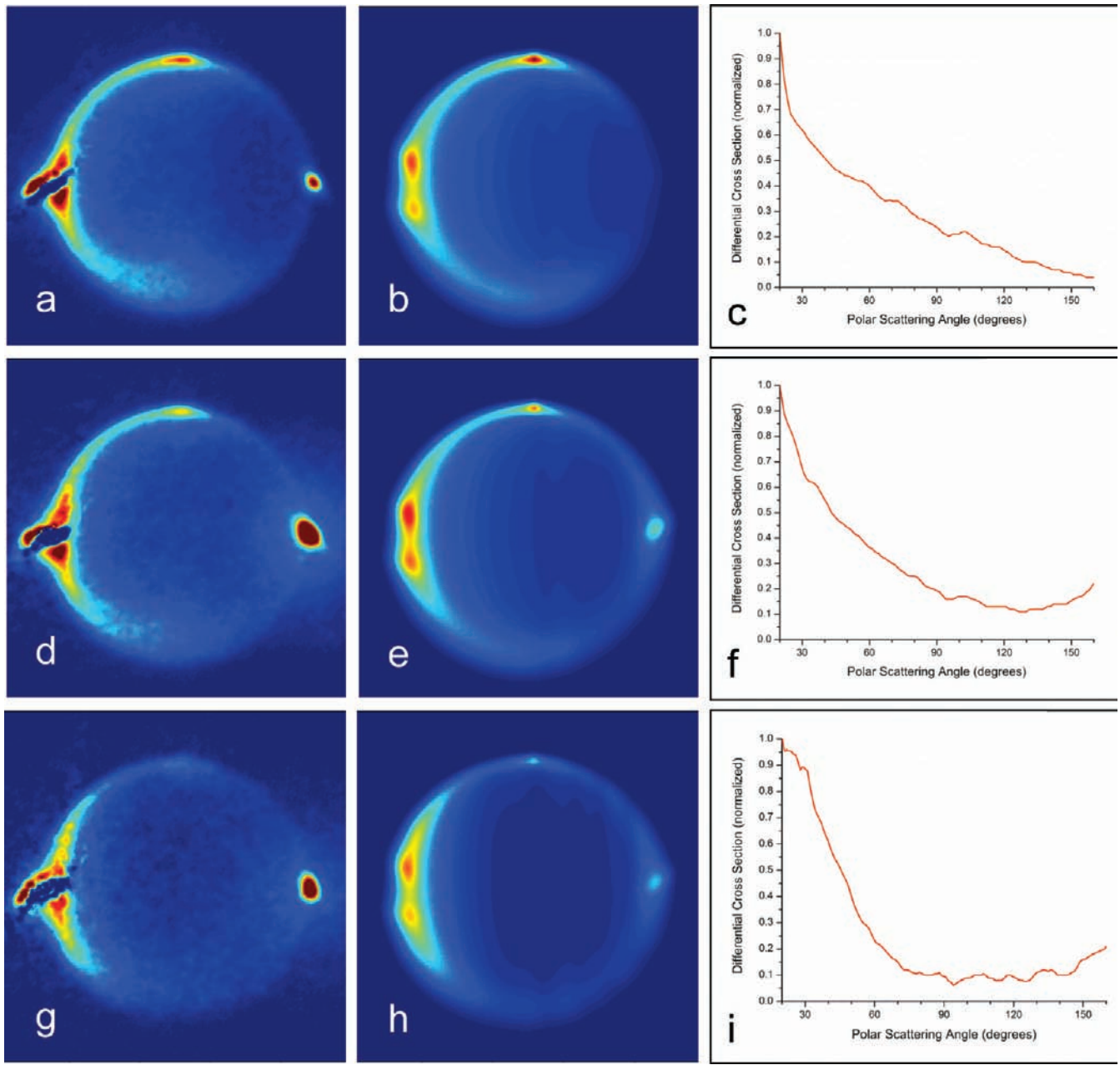

Figure 3. Experimental images, simulated images, and differential cross sections for ND_3/Ne scattering: (a)−(c) $J = 0$, $K = 0 \rightarrow J = 2$, $K = 0$; (d)−(f) $J = 1$, $K = 1 \rightarrow J = 2$, $K = 11$ (g)−(i): $J = 1$, $K = 1 \rightarrow J = 2$, $K = 2$.

actual differential cross section. This "trial" DCS is then fed back into the simulation to construct a realistic simulated image. The annular intensity of the experimental image is divided by the annular intensity of the simulated image, and gives a closer approximation to the actual differential cross section. This more accurate differential cross section is again fed back into the simulation for comparison with the experimental image, and the process is repeated until the simulated image matches the experimental image as closely as possible. To the extent that the instrument function is correct, this procedure yields the true differential cross section for the scattering process.

The instrument functions (for the first iteration of the extraction process), and simulated images (for subsequent iterations), are calculated in two steps. The first step involves the calculation of the three-dimensional center-of-mass velocity distribution of the scattered molecules from the measured velocity distributions of the parent molecular beams and the degree of rotational excitation of ND_3. A three-dimensional velocity array is constructed whose entries represent the number of molecules scattered at that particular velocity. The mesh spacing of the array is ~6 m/s, which is approximately equal to the velocity resolution of the experimental images. For the calculation of simulated images in the second and later steps of the extraction process, an additional weight factor is applied to each element of the three-dimensional velocity array using the trial differential cross section. For the calculation of the initial instrument function, the molecules are assumed to be scattered isotropically, and no additional weight factor is applied.

The second step involves weighing each element of the three-dimensional velocity array according to the efficiency with which those molecules are detected. A detection weight factor is calculated, which describes the spatial overlap of the detection laser beam with the spatial distribution of the scattered molecules at the instant they are ionized. We first divide the molecular beam pulses, which are assumed to be Gaussian in time, into 100 temporal subunits. For each temporal subunit, we then

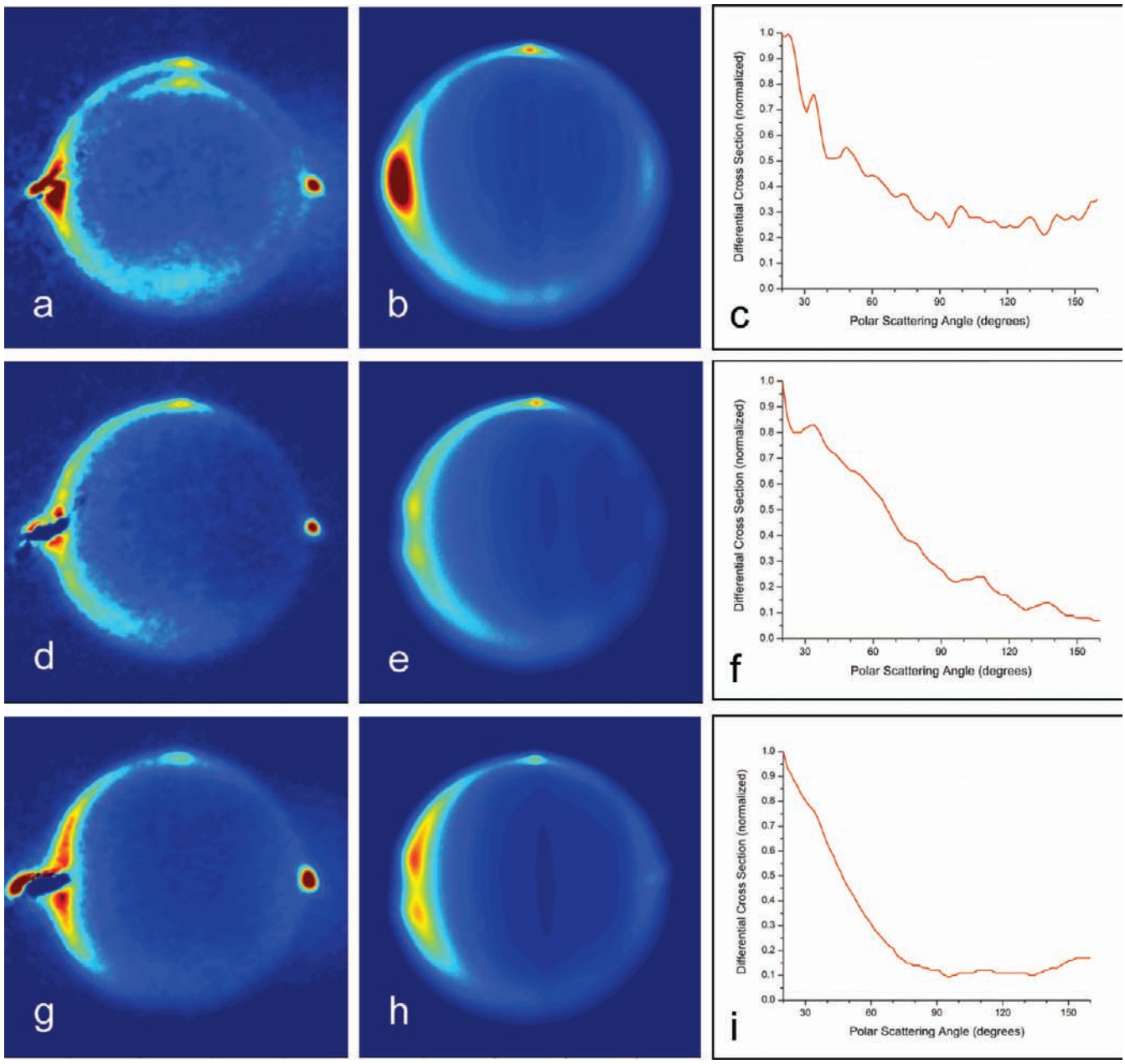

Figure 4. Experimental images, simulated images, and differential cross sections for ND_3/Ne scattering. The inner ring in (a) is due to an overlapping transition involving a rotational level with $J > 3$. (a)−(c): $J = 1$, $K = 1 \rightarrow J = 3$, $K = 1$; (d)−(f) $J = 1$, $K = 1 \rightarrow J = 3$, $K = 2$; (g)−(i) $J = 0$, $K = 0 \rightarrow J = 3$, $K = 3$.

calculate the spatial location of molecules moving at each velocity in the three-dimensional array at the moment of ionization, i.e., the distance each molecule travels from the center between the time it is scattered and the time it is detected. The laser intensity at each spatial location is then calculated and is used, in combination with the Doppler shift of the molecule and the frequency profile of the laser, to determine the ionization probability. (Molecules that have traveled further in the scattering plane than the radius of the aperture of the extraction optic, and are thus excluded from detection, are assigned an ionization probability of zero.) The sum over all temporal subunits is then calculated, giving an overall weight factor for each element of the original three-dimensional velocity array.

The detection weight factor is then combined with the velocity distribution from the first step of the calculation to give a weighted three-dimensional velocity distribution that reflects both the number of molecules moving at that velocity and the probability with which each molecule is ionized. (The structure of the array resembles, at this point, the actual spatial distribution of velocity-mapped ions just before reaching the detector.) To produce the final simulated image, we simply "crush" the distribution, i.e., calculate the sum of the weighted three-dimensional array over the vertical dimension. A Gaussian blur is applied to the simulated image to reflect imperfections in the experimental imaging system.

The process is summarized in Figure 2. Panel a shows the instrument function appropriate for $J = 0$, $K = 0 \rightarrow J = 3$, $K = 3$ scattering. The instrument function peaks at 90° and 270°, reflecting the higher detection sensitivity to molecules with very low laboratory-frame velocities and those propagating parallel to the laser axis. Panel b shows the intensity around an annulus centered on and encompassing the image, with an annular width of 20 pixels. Panel c shows the experimental image, and panel

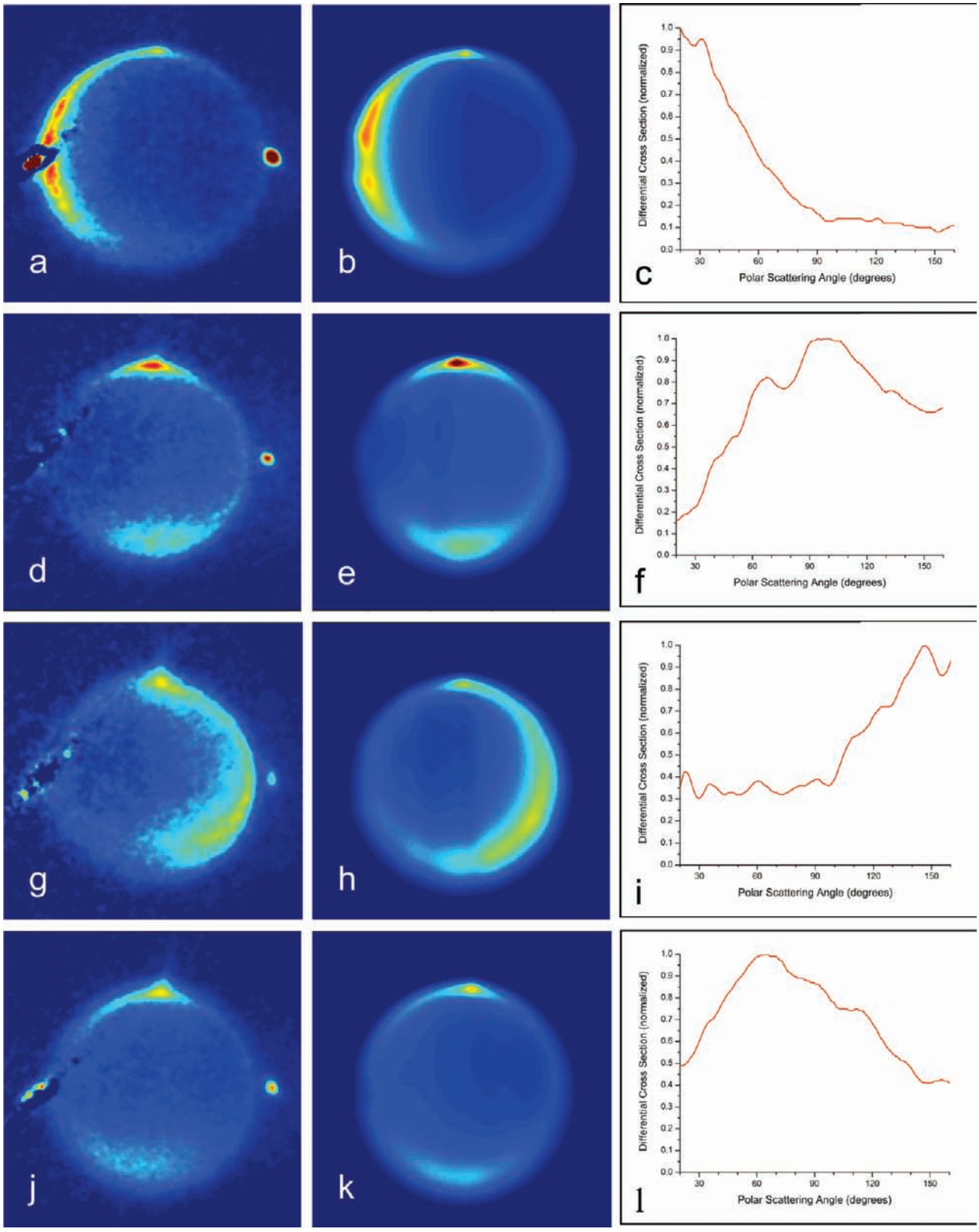

Figure 5. Experimental images, simulated images, and differential cross sections for ND_3/Ne scattering: (a)−(c) $J = 1$, $K = 1 \rightarrow J = 4$, $K = 4$; (d)−(f) $J = 0$, $K = 0 \rightarrow J = 5$, $K = 0$; (g)−(i) $J = 0$, $K = 0 \rightarrow J = 6$, $K = 3$; (j)−(l) $J = 1$, $K = 1 \rightarrow J = 7$, $K = 7$.

d shows the intensity around the same annular region as in panel b. The ratio of the annular intensities in (d) and (b) provides a trial differential cross section, which is used [along with the parameters used to create the instrument function in (a)] to create a simulated image. The annular intensities of the simulated and experimental images are then calculated, and their ratio provides an improved trial differential cross section, which is fed back into the simulation to provide an improved simulated image. The process is repeated until the agreement between the simulated and experimental images can no longer be improved. Amplification of high-frequency noise in the images is avoided by box-averaging the trial differential cross section, during each iteration of the extraction process, across a 5° angular window. The portions of the extracted differential cross sections between

0−20° and 160−180° are simply discarded, as these regions are partially overlapped by the "beam spots".

Experimental and simulated images are shown in Figures 3−5. Images of scattered molecules with $J = 2$ are shown in Figure 3, scattered molecules with $J = 3$ are shown in Figure 4, and molecules with $J \geq 4$ are shown in Figure 5. As seen in the figures, the extraction process reproduces nearly all of the features found in the experimental images. While the presence of rotationally excited molecules in the beams creates some interference near 0° and 180°, this creates only a local (±10°) disparity between the simulations and the experiment.

The extracted differential cross sections are shown in the right panel of each of the figures. Scattering generally shifts to larger angles as the difference in energy between the initial and final quantum states increases. Levels with $J = 2$ and $J = 3$ are primarily forward-scattered, but by $J = 3$ there is already significant scattering near 90°, and for $J = 5$ and above, the molecules are side-scattered or backscattered entirely. Although calculated differential cross sections for the ND_3/Ne system have not been reported, our observations here are qualitatively similar to the observations reported by Meyer[12,13] for the similar NH_3/He and NH_3/Ar systems, who interpreted the shift in the differential cross section toward larger angles with increasing ΔJ in terms of a rotational rainbow. As Meyer notes, the observation of both small- and large-angle scattering means that the data set is sensitive to collisions across a wide range of impact parameters, which affords sensitivity to a large region of the electronic potential energy surface.

Before concluding, we wish to mention briefly the impact of the differential cross section on the production of slow-moving molecules. As we have recently shown,[19] a subset of the ND_3 molecules that undergo inelastic collisions with Ne are slowed to speeds ranging from 21 to 32 m/s (8 to 27 m/s calculated) depending on the final rotational state. (As ND_3 and Ne have identical masses, the slowest molecules occur with the smallest change in rotational energy; only elastic collisions produce truly stationary molecules for this system.) At the velocities used in these experiments, the slowest molecules are those scattered near $\theta = 90°$. For the rotational states in question, however, the differential cross section at this scattering angle is rather low; the differential cross section is much higher at shallower angles ($\theta < 45°$). It is possible to take advantage of the larger cross section at smaller angles and enhance the number of slow molecules by "tilting" the Newton sphere.[15,16,19] This can be accomplished by lowering the velocity of ND_3 and/or raising the velocity of Ne, such that the laboratory-frame origin lies at a lower scattering angle. Simply seeding the ND_3 in Kr, for example, shifts the laboratory-frame origin to $\theta = 65°$ and produces a dramatic increase in the number of slowed molecules.[19] The number of slow molecules can be increased further by increasing the velocity of Ne by seeding in He.

IV. Conclusions

We report the first measured differential cross sections for rotationally inelastic collisions between ND_3 and Ne, obtained using the velocity-mapped ion imaging technique. Our observations compare well with and complement previous observations from rotationally inelastic scattering experiments involving the similar NH_3/He and NH_3/Ar systems and will allow further comparison between theory and experiment for the ammonia/rare gas system.

Acknowledgment. We acknowledge Mr. Mark Jaska for technical support. Funding for this work was provided by the U.S. Department of Energy, Office of Basic Energy Science. Sandia is a multiprogram laboratory operated by Sandia Corportation, a Lockheed Martin Co., for the U.S. Department of Energy.

References and Notes

(1) Heck, A. J. R.; Chandler, D. W. *Annu. Rev. Phys. Chem.* **1995**, *46*, 335.
(2) Eppink, A. T. J.; Parker, D. H. *Rev. Sci. Instrum.* **1997**, *68*, 3477.
(3) Suits, A. G.; Bontuyan, L. S.; Houston, P. L.; Whitaker, B. J. *J. Chem. Phys.* **1992**, *96*, 8618.
(4) Ashfold, M. N. R.; Nahler, N. H.; Orr-Ewing, A. J.; Vieuxmaire, O. P. J.; Toomes, R. L.; Kitsopoulos, T. N.; Garcia, I. A.; Chestakov, D. A.; Wu, S.-M.; Parker, D. H. *Phys. Chem. Chem. Phys.* **2006**, *8*, 26.
(5) Kohguchi, H.; Suzuki, T.; Alexander, M. H. *Science* **2001**, *294*, 832.
(6) Garand, E.; Zhou, J.; Manolopoulos, D. E.; Alexander, M. H.; Neumark, D. M. *Science* **2008**, *319*, 72.
(7) Kłos, J.; Aoiz, F. J.; Verdasco, J. E.; Brouard, M.; Marinakis, S.; Stolte, S. *J. Chem. Phys.* **2007**, *127*, 031102.
(8) Gijsbertsen, A.; Linnartz, H.; Stolte, S. *J. Chem. Phys.* **2006**, *125*, 133112.
(9) Lorenz, K. T.; Westley, M. S.; Chandler, D. W. *Phys. Chem. Chem. Phys.* **2000**, *2*, 481.
(10) Wade, E. A.; Lorenz, K. T.; Springfield, J. L.; Chandler, D. W. *J. Phys. Chem. A* **2003**, *107*, 4976.
(11) McBane, G. C. Simulation and Analysis of Image Data from Crossed Beam Experiments. In *Imaging in Chemical Dynamics*; Suits, A. G., Continetti, R. E., Eds.; American Chemical Society: Washington, DC, 2000.
(12) Meyer, H. *J. Chem. Phys.* **1994**, *101*, 6697.
(13) Meyer, H. *J. Phys. Chem.* **1995**, *99*, 1101.
(14) van der Sanden, G. C. M.; Wormer, P. E. S.; van der Avoird, A. *J. Chem. Phys.* **1996**, *105*, 3079.
(15) Elioff, M. S.; Valentini, J. J.; Chandler, D. W. *Science* **2003**, *302*, 1940.
(16) Elioff, M. S.; Valentini, J. J.; Chandler, D. W. *Eur. Phys. J. D* **2004**, *31*, 385.
(17) Strecker K. E. Chandler D. W. In *Low Temperatures and Cold Molecules*; Smith I. W., Ed.; World Scientific: Singapore, 2008.
(18) Strecker, K. E.; Chandler, D. W. *Phys. Rev. A* **2008**, *78*, 063406.
(19) Kay, J. J. van de Meerakker, S. Y. T. Strecker, K. E. Chandler, D. W. *Faraday Discuss.*, **2009**, *142* 143 DOI: 10.1039/B819256C.
(20) Ashfold, M. N. R.; Dixon, R. N.; Stickland, R. J.; Western, C. M. *Chem. Phys. Lett.* **1987**, *138*, 201.
(21) Ashfold, M. N. R.; Dixon, R. N.; Little, N.; Stickland, R. J.; Western, C. M. *J. Chem. Phys.* **1988**, *89*, 1754.

JP904983W